Random Walk Theory Applied to Electron Avalanche Formation

Gerald W. Englert

Lewis Research Center, National Aeronautics and Space Adiministration
Cleveland, Ohio, U.S.A.

(Z. Naturforsch. **29 a**, 51–64 [1974]; received 20 August 1973)

Use of microscopic detail in random walk theory describing the initial formations of a large number of avalanches show that concomitant electron transport coefficients quickly relax to equilibrium values. This enables the use of random walks having step sizes and probabilities based only on local electric field strengths and densities. A self-consistent avalanche solution which accounts for collective long range Coulomb interactions as well as short range elastic and inelastic collisions between electrons and background atoms is demonstrated for helium. Avalanche growth retardation followed by an abrupt growth augmentation as time proceeds is shown to be associated with the formation of regions of charge density extrema near the avalanche axis and within the axial distance covered by the electron swarm.

Introduction

The abrupt spacial and timewise variation of avalanche structure renders detailed theory as well as experiment difficult. A means of investigating theoretical models which allows incorporation of considerable physical detail could be quite useful.

Random walk theory has been employed in the computer simulation of the microscopic details of electron motion [1]. In this procedure the trajectory of each electron is followed as it experiences both elastic and inelastic short range collisions with background neutral particles, and as it is acted upon by the electric field in the time between collisions. The details of each collision are based on random selection of values from sets of numbers distributed in accordance with cross section data. A constant number (representative sampling) of electrons are followed to study a process having a uniform density.

In avalanche formation, however, an additional electron (therefore walk) originates at each ionizing collision. The density of charged particles reaches values such that long range Colulomb interactions must be included. Since more than 10^8 ionizations usually occur in the development up to the streamer formation stage, computer time expenditure for such detailed calculations becomes a serious problem.

When a large number of microscopic events occur within small macroscopic volume and time increments, the step sizes and probabilities used in the random walk (RW) can be based on local averages. This technique, which has been used to simulate a pertinent class of parabolic nonlinear differential equations [2, 3] considerably facilitates the calculation procedure. Application of such a macroscopic technique to the electron avalanche while preserving the microscopic detail and obtaining a self-consistent solution to the internal electric fields was therefore undertaken.

The avalanches of the present investigation are the type which are formed independent of secondary ionizations (wall effects). This is the case where the space charge of the avalanche itself is effective in streamer formation [4]. Numerical results were obtained for avalanche formation in helium, at ratios of external electric field to background pressure of 20, 30, and 40 V/cm-torr. Electronic excitation by electron impact is included, however, photoionization and metastables were found to have little effect on this type of avalanche and were excluded. Such processes, at most, would serve only to alter the effective first Townsend ionization coefficient [5].

Microscopic RW

The detailed RW procedure was applied to the early stages of formation of a large number of electron avalanches in helium. Typical patterns of the locations of the electrons and ions at various formation times are shown in the computer plots of Figure 1. The external electric field is in the negative z direction.

The electrons move as a spherical swarm. The ion pattern is typical of that observed in cloud chamber photographs. These avalanches were started with a number of electrons, N_0, considerably greater than one to provide larger statistical samples. The plots can also be considered to represent a superposition of N_0 avalanches, each starting with one electron

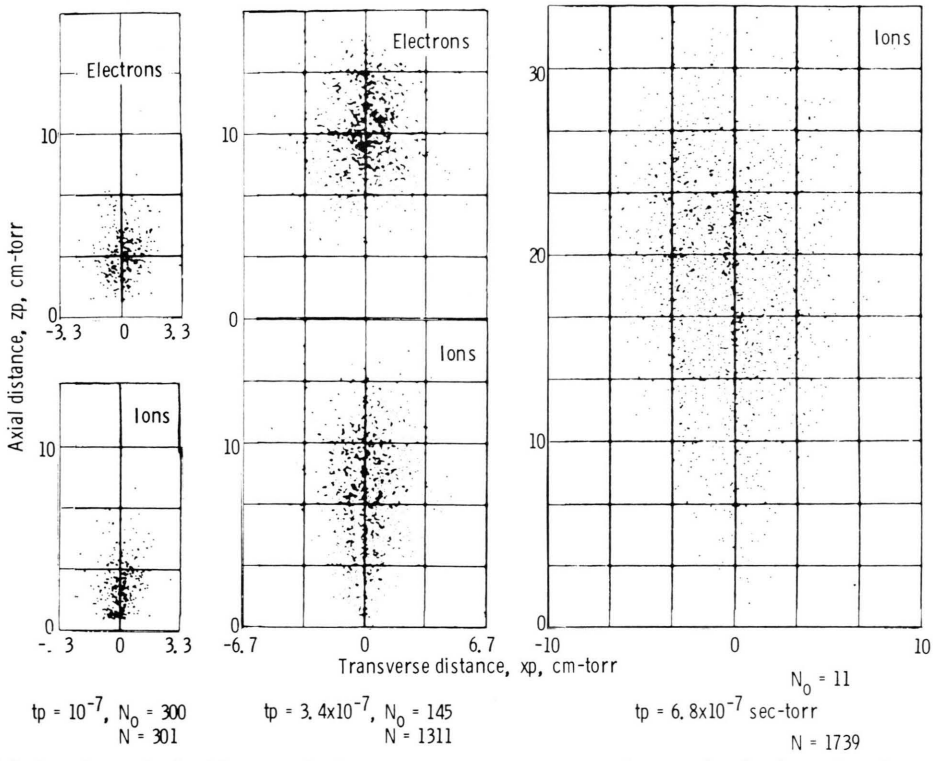

Fig. 1. Particle locations, obtained by use of microscopic RW procedure, at three avalanche formation times, *tp*, in helium. Lower plots are ion locations; upper two plots show electron swarms. Listed also are number of superimposed avalanches, N_0, and the number of ionizations, N. $E/p=30$ V/cm-torr.

thus giving a representative average of formations which deviate considerably in the early time periods.

The electron energy distributions relaxed quite independent of various initial energies to a terminal steady state in short generalized time periods, tp, close to those found in an earlier investigation [1] for a fixed number of electrons [6].

Of the electron transport coefficients needed later in this study, the Townsend first ionization coefficient, α_T, is the most sensitive to the electron energy and was therefore selected for presentation. How α_T/p is influenced by the initial energy, ε_0, of the first electron of each avalanche is shown on Figure 2. Values of ε_0 were arbitrarily selected at 1/2 and 3/2 of the ionization potential of helium ($V_i = 24.46$ eV). Data points represent an average of 1000 avalanches. Illustrated also is the scatter in the data due to differences in the averages of 3 groups of 300 avalanches. With $\varepsilon_0 < V_i$ little scatter is observed until a significant number of electrons reach energies sufficient to cause ionizations. Scatter is again reduced as equilibrium energy distributions are attained. Time for the transport coefficients to reach

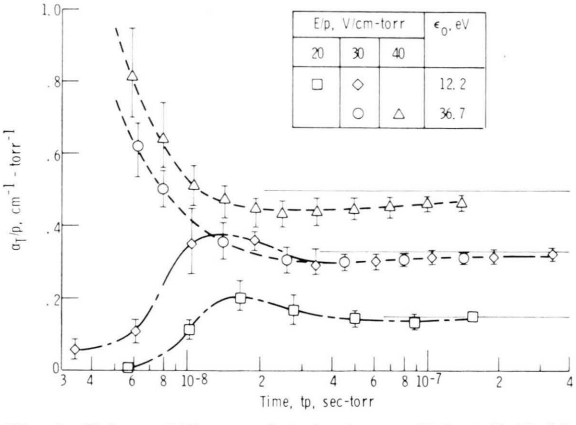

Fig. 2. Values of Townsend ionization coefficient divided by pressure, α_T/p, as electron energy varies from an initial value to a terminal distribution. Solid horizontal lines denote terminal steady state values of α_T/p of Ref. 1 starting at the relaxation time of Eq. (1) of Reference 1.

equilibrium values is about one-hundredth the time of formation of fully developed avalanches [7].

It requires, for example, approximately 10 minutes of time on the IBM 7094 digital computer to determine formations in which the order of 10^3 ioni-

zation events occur. The number of ions in avalanches developed up to the streamer stage may reach the order of 10^{10}. Use of this detailed microscopic type of RW procedure would thus require far excessive amounts of computer time during such long time periods. Fortunately this is where the use of equilibrium values of transport coefficients are justified. The electron motion can then be described by the electron transport equation (see Appendix) the solution of which is simulated by a RW procedure. Step sizes and probabilities in this macroscopic type RW are functions only of the local electric field and background density of neutrals. The electron transport equation is coupled with the ion motion through Poisson's equation.

Macroscopic RW

Since the macroscopic descriptions afforded by the transport equations apply to the electron avalanche, the concept of a random walk on a three-dimensional grid [2, 3] can be used to simplify the computer simulation process. In this procedure the step sizes and probabilities of taking steps in the various directions are expressed as local averages which can be determined in terms of transport coefficients. The equations describing such a RW is

$$\frac{\partial W}{\partial t} = \sum_{j=1}^{3} \left\{ \frac{\partial [(P_j^+ - P_j^-) W]}{\partial X_j} \frac{\Delta X_j}{\Delta t} + \frac{1}{2} \frac{\partial^2 W}{\partial X_j^2} \frac{(\Delta X_j)^2}{\Delta t} \right\}. \tag{1}$$

This equation, based on the law of compound probability, is essentially a law of conservation of particles as they move to and from neighboring points on a three-dimensional lattice (Figure 3). The components of the step sizes, ΔX_j, are the grid spaces. The terms P_j^+ and P_j^- are the probabilities of taking steps in the positive and negative directions along the j^{th} coordinate. It is assumed that each of the three components of the steps contribute to the particle movement for each time increment, Δt. Then

$$P_j^+ + P_j^- = 1, \quad j = 1, 2, 3, \tag{2}$$

which corresponds to steps across diagonals of the lattice.

Let X_j, $j = 1, 2, 3$ be cartesian coordinates. Then W, which is the probability density of particles being at a certain grid location at time t, can simply be set equal to the density of electrons, n_e.

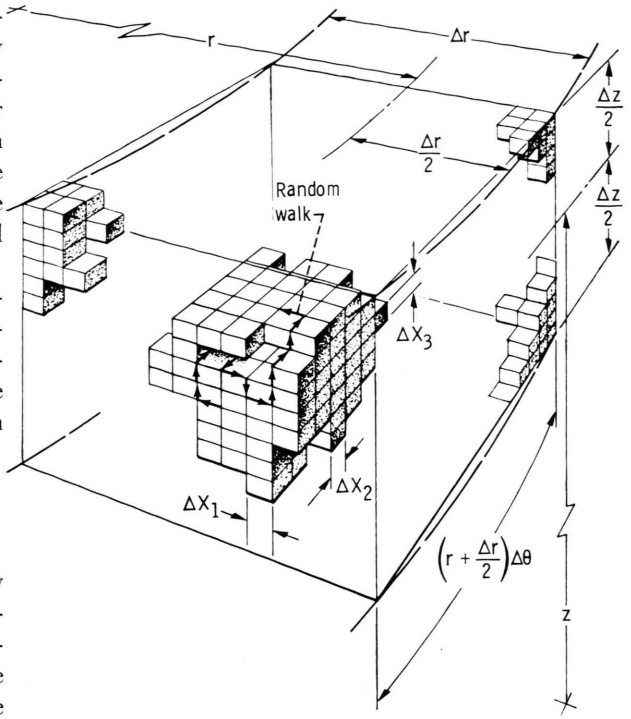

Fig. 3. Random walk on a three-dimensional rectangular grid. Division of space into larger cylindrical zones, for tallying purposes and internal field calculation, is shown by dashed lines. Axial distance, z, is measured from the initial location of the first electron. Radial distance, r, is measured from the avalanche axis.

The components of step size, ΔX_j, are identifiable with second moments, or root mean squared averages, of the components of microscopic distance, Δx_j, between collisions. Letting a bar denote average,

$$\Delta X_j = \sqrt{\overline{(\Delta x_j)^2}}, \quad j = 1, 2, 3. \tag{3}$$

Then using the definition of diffusion coefficient,

$$D_j = \overline{\Delta x_j^2}/2\tau,$$

it follows that

$$\Delta X_j = \sqrt{2 D_j \tau}, \quad j = 1, 2, 3. \tag{4}$$

The mean free time between collisions, τ, is equivalent to Δt. For helium, τ can be approximated by [1]

$$\tau = 1/(n Q_a v). \tag{5}$$

This is because the product of electron velocity with Q_a is very nearly constant over the range of interest herein. Here Q_a is the total absorption cross section of electrons colliding with neutral background (helium) atoms of density n. Setting v equal to $\sqrt{2\bar{\varepsilon}/m}$, where $\bar{\varepsilon}$ is the mean electron energy of Ref. [1], for

the macroscopic RW gives the very small variation of τ with E/p shown in Figure 4.

The bias, $P_j^+ - P_j^-$, can be used to describe the influence of a preferred direction of velocity, which involves a first moment of Δx_j

$$P_j^+ - P_j^- = \overline{\Delta x_j} \Big/ \sqrt{\overline{(\Delta x_j)^2}} = v_{\mathrm{d},j}\,\tau / \sqrt{2\,D_j\,\tau}\,, \quad j = 1, 2, 3. \tag{6}$$

In this case the velocity is that of the electron drift.

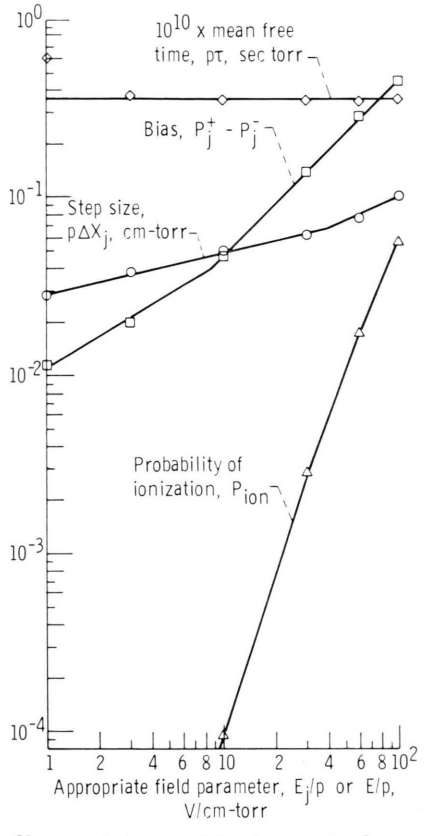

Fig. 4. Characteristic quantities for use in the macroscopic RW of electrons in helium. Data points were calculated from transport coefficients of Reference 1. Lines denote empirical curve fits used in the computer program. When determining bias, use E_j/p as the abscissa.

Diffusion in the presence of an electric field has a nearly constant coefficient over the range of E/p of most concern in this investigation [1]. It will be assumed, therefore, that step size is isotropic and only weakly dependent on space, although it can be strongly time dependent. Using Eqs. (4) and (6) in (1) and identifying W with n_e then yields

$$\partial n_e/\partial t = -\nabla \cdot n_e \boldsymbol{v}_d + D\nabla^2 n_e\,. \tag{7}$$

Consider ionizing events to occur during the RW with a probability per collision, P_{ion}. The rate of ionizing events per unit volume is then $P_{ion}\,n_e/\tau$. This is equivalent to $\alpha_T\,v_d\,n_e$ where α_T is the Townsend first ionization coefficient. Thus

$$P_{ion} = \alpha_T\,v_d\,\tau\,. \tag{8}$$

Eq. (7), extended to include this source term, becomes

$$\partial n_e/\partial t = -\nabla \cdot n_e \boldsymbol{v}_d + D\nabla^2 n_e + \alpha_T\,v_d\,n_e\,. \tag{9}$$

This is equivalent to the electron transport equation (see Appendix) within the spacial restriction on step size (and thus on D for constant τ) which will be appraised later.

Performance of RW-on-a-Grid

Step sizes and probabilities used in the macroscopic RW are plotted in Figure 4. These are based on equilibrium transport coefficients of the author [1] and Eqs. (4), (6), and (8). This information was stored in the computer by means of the cruve fits shown by the lines through the data.

In the execution of each step of the random walks four numbers are drawn at random from a set of numbers uniformly distributed over the interval from 0 to 1. Such sets of random numbers are available in most computer libraries. Three of these numbers are used to determine step direction. For example, if the j^{th} random number is less than the corresponding P_j^+, the component of the step along the j^{th} coordinate is considered to be positive. Here P_j^+, obtained by combining Eqs. (2) and (6) can be conveniently written as

$$P_j^+ = 1/2 + v_{\mathrm{d},j}\sqrt{\tau/8D}\,.$$

The fourth random number is compared with P_{ion}, and if less than P_{ion}, an ionization event is assumed to occur.

Only the electrons have appreciable diffusive motion or cause ionizations, and are, therefore, random walked. It is sufficient to merely include the drift motion of the ions in the calculations.

At the end, t_k, of various macroscopic time periods the locations of the electrons and ions are recorded for plotting (as in Fig. 1) and also tallied to determine their distributions in space. At these t_k the probabilities and step sizes are determined over the space of immediate interest, and the resulting values stored in matrix form for convenient access

during the following walks. In the early formation period of the avalanche ($N_e < 10^6$) the internal (induced) electric field is negligible and the electron transport coefficients, thus probabilities and step sizes, are constants. As the formation proceeds, the permissible lengths of the time periods become smaller. At each t_k the electric field of the avalanche is determined by numerical integration over the distributions of electrons and ions. Thus a self-consistent description of collective interactions of charged particles among themselves and with the electric field is obtained. As the magnitude of the internal field reaches and goes beyond that of the external field, the Δt_k periods must be kept very small (of the order of $10\,\tau$).

The RW can be further facilitated by scaling these quantities by a constant factor A as

$$\Delta X_j' = \sqrt{A}\,\Delta X_j\,,$$

$$P_j^{+\prime} - P_j^{-\prime} = \sqrt{A}\,(P_j^{+} - P_j^{-})\,,$$

$$P'_{\text{ion}} = A\,P'_{\text{ion}}\,,$$

and

$$\tau' = A\,\tau\,.$$

Then, by Eqs. (4), (6), and (8), the transport coefficients, and thus the RW results, remain the same, while permitting use of a smaller number of larger steps. Scale factors much greater than one are permissible only where the avalanche structure is changing slowly with respect to time and distance. In any event $P_j^{+\prime}$ and P'_{ion} must be kept less than unity.

Computing time can now be reduced to about 10^{-3} of that required in the microscopic RW. Nevertheless, this time once more becomes excessive for avalanche formations resulting from more than 10^7 ionizations. With such a large number of electrons in the swarm, however, it is not necessary to walk each one. At the higher t_k, samplings of about 3×10^3 "test" electrons were found sufficient to represent the avalanche growth. Each of such test electrons randomly selected from the spacial distributions at t_k generates a subavalanche over the period $t_{k+1} - t_k$. The resulting distributions are weighted for the actual number of electrons and ions being represented. In this manner the RW process can be continued through the final formation periods with, for example, total time expenditure on an IBM 7094 computer of the order of 10^2 minutes.

Determination of Internal Electric Field

Axial symmetry is assumed in the determination of the electric field from the tallies of the electrons and ions. The induced electrostatic potential for single charged ions can be written as

$$\Phi(r,z) = e \int\int \cdot \int \frac{n_i(r',z') - n_e(r',z')}{\sqrt{r^2 + r'^2 - 2\,r\,r'\cos\Theta + (z-z')^2}}\, r'\,\mathrm{d}r'\,\mathrm{d}\Theta\,\mathrm{d}z' \tag{10}$$

where $\Theta = \theta - \theta'$. Integration is over the whole space occupied by the avalanche except for a cut-off at the minimum distance between the field and source points, which was set at $n_e^{-1/3}$. By differentiation similar expressions can be obtained for the induced electric field components, E_r and E_z. The integration over θ can be expressed in terms of elliptic integrals as

$$\Phi = 4\,e\,\{\iint[(n_i - n_e)/\sqrt{2\,b}]\,\mathcal{F}(\gamma, \Gamma^{-1})\,r'\,\mathrm{d}r'\,\mathrm{d}z' + \iint[(n_i - n_e)/\sqrt{a+b}]\,\mathcal{K}(\Gamma)\,r'\,\mathrm{d}r'\,\mathrm{d}z'\} \tag{11}$$

where

$$a = r^2 + r'^2 + (z-z')^2\,,\quad b = 2\,r\,r'\,,$$

$$\Gamma = \sqrt{2\,b/(a+b)}\,,$$

$$\gamma = \arcsin\sqrt{b\,(1+\cos\delta\theta)/(a+b)}\,.$$

The distance of closest approach in the θ direction is denoted by $\delta\theta$. The first integral in Eq. (11) represents integration over the part of the surce distribution which is located in the neighborhood of the field point, where a cut off of θ is required. The second integral is over the remaining part of the source distribution.

The r', z' space as well as the field space is broken into small annular volume elements. Source densities are assumed constant in such rings of volume equal to $2\pi r'\,\Delta r'\,\Delta z'$. The quantities Φ, E_r, E_z are considered constant in similar field space elements. The final expressions, written for use in matrix form, are

$$\Phi(l,m) = (e/\pi) \cdot \left\{[N_i(l,m) - N_e(l,m)]\,r^{-1}\ln\operatorname{tn}\left(\frac{\gamma}{2} + \frac{\pi}{4}\right) + 2\sum_{j,k=1}^{20}{}' \frac{[N_i(j,k) - N_e(j,k)]}{\sqrt{a+b}}\,\mathcal{K}(\Gamma)\right. \tag{12}$$

$$E_r(l,m) = (e/2\pi) \cdot \left\{ [N_i(l,m) - N_e(l,m)]\, r^{-2} \ln \operatorname{tn}\left(\frac{\gamma}{2} + \frac{\pi}{4}\right) + 4 \sum_{j,k=1}^{20,\prime} \frac{N_i(j,k) - N_e(j,k)}{b\sqrt{a+b}} \cdot \left[\frac{b\,r - a\,r'}{a-b}\, \mathcal{E}(\Gamma) + r'\, \mathcal{K}(\Gamma) \right] \right\} \qquad (13)$$

and

$$E_z(l,m) = (e/4\pi) \cdot \left\{ [N_i(l,m) - N_e(l,m)]\, r^{-3}\, n_e^{-1/3} \ln \operatorname{tn}\left(\frac{\gamma}{2} + \frac{\pi}{4}\right) + 8 \sum_{j,k=1}^{20,\prime} \frac{N_i(j,k) - N_e(j,k)}{(a-b)\sqrt{a+b}} (z-z')\, \mathcal{E}(\Gamma) \right\} \qquad (14)$$

where for small $r - r'$ and $z - z'$,

$$\mathcal{F}(\gamma, \Gamma^{-1}) \approx \ln \operatorname{tn}\left(\frac{\gamma}{2} + \frac{\pi}{4}\right)$$

$$\mathcal{E}(\gamma, \Gamma^{-1}) \approx \sqrt{(1 + \cos \delta\theta)/2}\,.$$

The prime marks on the summation signs indicate exclusion of $j = l$ and $k = m$ combinations.

Formation over an Extended Time Period

Only one macroscopic avalanche for each external field, E/p, value was computed up to the final stages of formation time, although several more were computed to intermediate stages of development. The ones selected for completion to final stages had initial growth rates closely approximating the average of the large number of microscopic avalanches previously calculated at corresponding E/p values. All of the macroscopic avalanches exhibited much the same details of development. Computer time expenditure would have been excessive to make a study of statistical variation. Since the macroscopic RW is based on transport coefficients, which are already averages of microscopic quantitees, it is apparent that less deviation between avalanches would result than obtained by the microscopic RW procedure.

Plots of the ion locations in fully developed avalanches, at E/p values of 20, 30, and 40 V/cm-torr, are presented on the left side of Figure 5. Better definition of avalanche profile is obtained by plotting z versus radial distance, r, instead of x. This makes more points visible in the outer boundary region due to the scale factor r in the equation

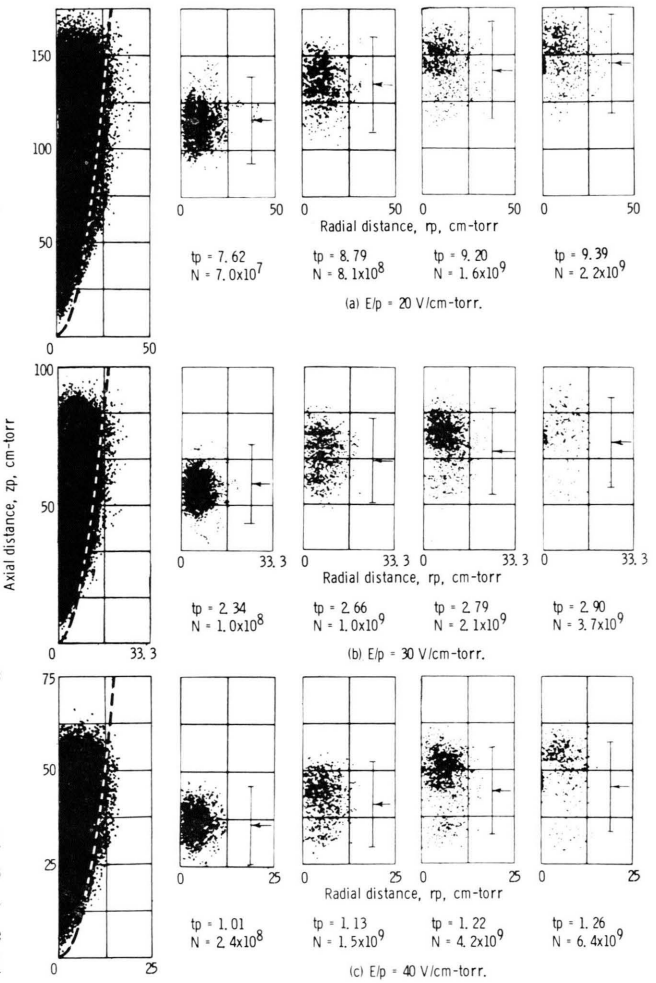

Fig. 5. Particle locations, obtained by the RW procedure, in helium. On the left side are three fully developed ion formations. The dashed lines represent $rp = 2r_D p = 4p\sqrt{Dz/v_d}$. Next are shown electron swarms at four times tp, given in μ-sec torr, at which the avalanche growth has reached the number of ions, N. Only a small fraction of the particles is plotted. Verticle lines give the axial distance $\pm 4p\sqrt{Dt}$ from $zp = v_d\, tp$ (denoted by arrows).
(a) E/p=20 V/cm-torr, (b) E/p=30 V/cm-torr,
(c) E/p=40 V/cm-torr.

$$n(r,z) = \int_0^{2\pi} n(r,\theta,z)\, r\, d\theta\,.$$

Twice the diffusion radius, $2r_D = 4\sqrt{Dz/v_d}$, shown by the dashed line, fairly well defines the boundary.

The corresponding electron swarms are shown at four time periods. The swarms span distances close to $4r_D$. They are nearly spherical at the first time period since the internal electric field is then quite small. The center is close to the axial location $z = v_d\, t$.

At the second time period the magnitude of the induced electric field is about one-third that of the external field and its presence is noticeable in the electron swarm pattern.

By the third time period, the internal field reaches peak values about equal to the external field value and its influence is very apparent in the electron pattern. At an external field, E/p, of 30 V/cm-torr, for example, local minimum and maximum values of total electric field occur at zp values of approximately 58 and 75 cm-torr, respectively. The concentration of electrons is quite strongly correlated to such field points since α_T, and thus the formation of new electrons and ions is exponentially dependent on field strength.

As the avalanche build-up continues beyond the third time period, the induced electric field strength near the axis and in the vicinity of $zp = v_d\, tp$ increases to magnitudes beyond the external field strength. The last plots on Fig. 5 show that there is a corresponding large concentration of ions and electrons at this location. In fact, the density is so high at the fourth time period that only a small sample of electrons could be plotted without a glare in this zone on the plotting screen obscuring details.

Contour plots of the ion and electron densities are shown in Fig. 6 at a formation time of 2.44 μ-sec torr for an external field of 30 V/cm-torr. The RW results (Fig. 6 a) compare quite well with constant coefficient theory (Fig. 6 b) at this tp where the induced electric field is considerably less than the external field. The diffusion radius profile, $2r_D$, is also shown on the RW ion plot. The exponential fall-off of ion, as well as electron, density from the peak regions near $z = v_d\, t$ and $r = 0$ is apparent.

In order to allow a space saving in plotting, marginal distributions, in which integration is over all dimensions except the one being studied are used to present the effects of the internal electric field on density distribution. Such plots preserve the essential features of interest and are shown for both charge species in Figs. 7 and 8 at various formation times and at an E/p of 30 V/cm-torr. The marginal distributions ($n_{j,r}$ and $n_{j,z}$) for the j^{th} charge species in the r and z directions, respectively, are normalized by dividing by $\exp(\alpha_T v_d t)$ yielding

$$F_{j,r} = n_{j,r} \exp(-\alpha_T v_d t) \equiv \exp(-\alpha_T v_d t) \int_0^\infty \int_0^{2\pi} \cdot n_j(r, \theta, z)\, r\, d\theta\, dz \qquad (15)$$

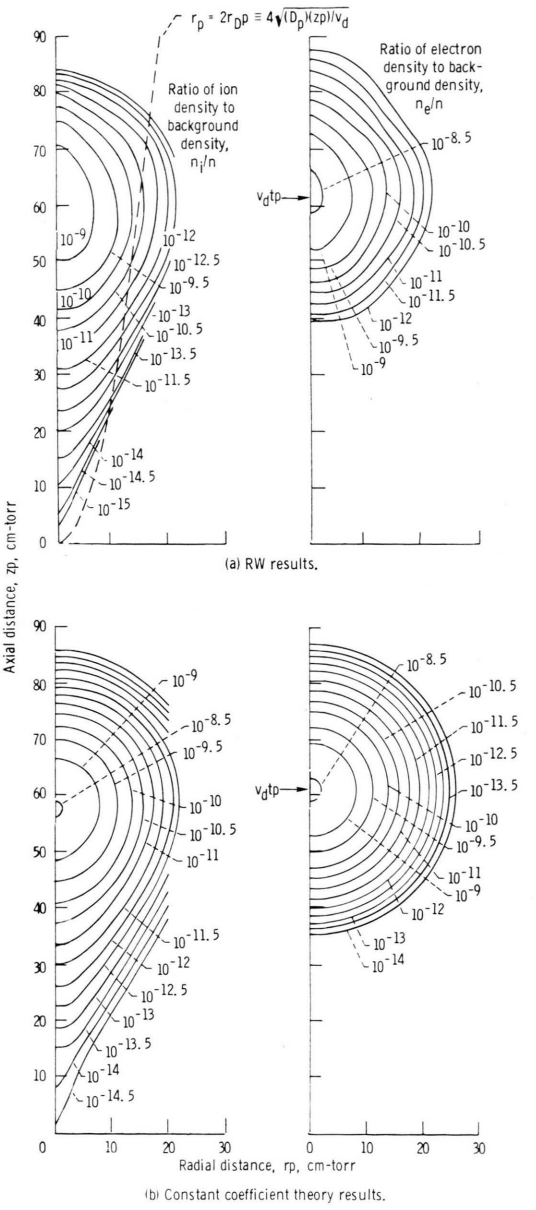

Fig. 6. Contour plots of ion and electron density divided by background density, n, of helium at a formation time, tp, of 2.44 μ-sec torr. The dashed line represents $rp = 2\, r_D\, p$. External electric field, E/p, is 30 V/cm-torr.
(a) RW results, (b) Constant coefficient theory results.

and

$$F_{j,z} = n_{j,z} \exp(-\alpha_T v_d t) \equiv \exp(-\alpha_T v_d t) \cdot \int_0^\infty \int_0^{2\pi} n_j(r, \theta, z)\, r\, d\theta\, dr\,. \qquad (16)$$

Keeping the scale factor r with the integration over θ in Eq. (15) makes the plots of $F_{j,r}$ versus r more

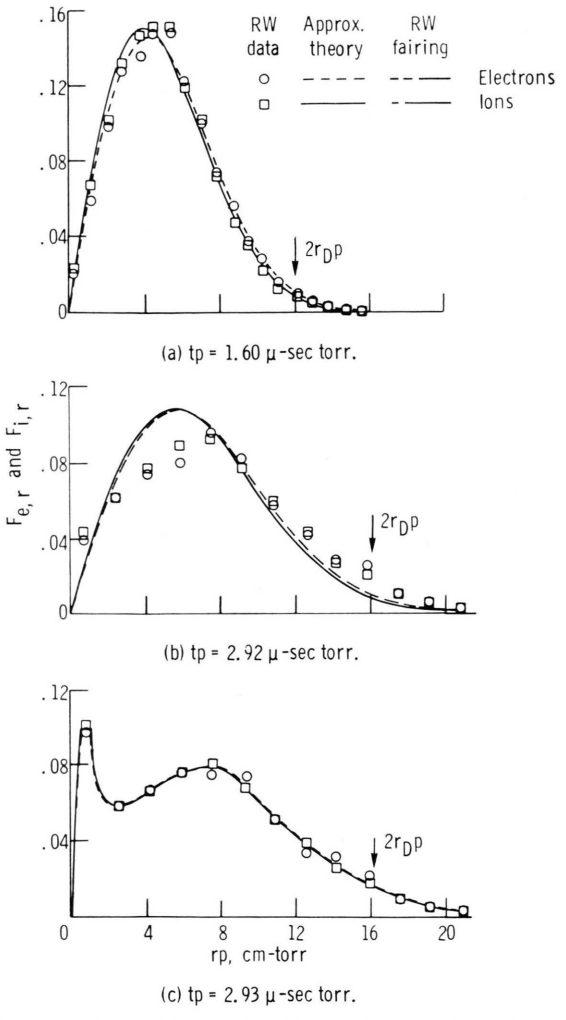

Fig. 7. Marginal density distributions in the radial direction at various formation times. The effective Townsend ionization coefficient, $(\alpha_T/p)_{eff}$, used in the theory of parts (a) and (b) is 0.317 and 0.305 cm^{-1} $torr^{-1}$, respectively. E/p= 30 cm-torr.
(a) $tp = 1.60$ μ-sec torr, (b) $tp = 2.92$ μ-sec torr, (c) $tp = 2.93$ μ-sec torr.

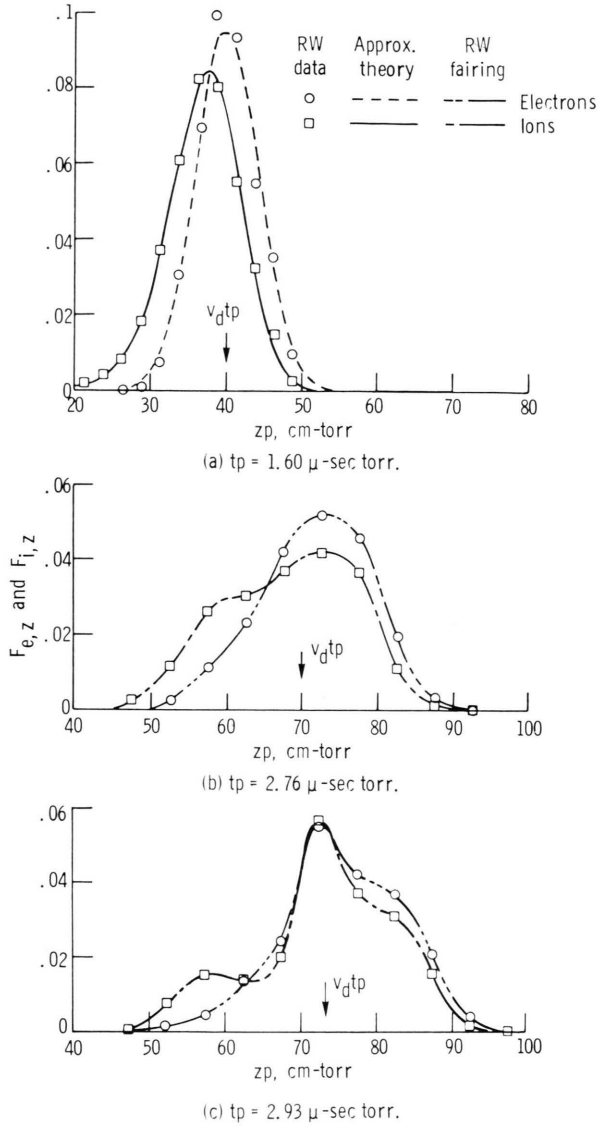

Fig. 8. Marginal density distributions in the axial direction at various formation times. The value of $(\alpha_T/p)_{eff}$ used in the theory of part (a) is 0.317 cm^{-1} $torr^{-1}$. E/p=30 V/cm-torr.
(a) $tp = 1.60$ μ-sec torr, (b) $tp = 2.76$ μ-sec torr, (c) tp=2.93 μ-sec-torr.

manageable as it reduces the otherwise exceptionally high values near $r = 0$. Theoretical values of $n_{j,r}$ and $n_{j,z}$ are given in Eqs. (A6) through (A9) of the Appendix.

When the induced electric field is negligible, so that the transport coefficients are constant, the constant coefficient theory agrees well with the RW results, as expected [Fig. 7(a) and 8(a)]. The electron axial distribution, at low formation times, peaks where z is equal to $v_d t$. The ion axial distribution peaks at only a slightly lower z since most of the ions are formed at the latter part of any given macroscopic time period where the number of electrons to do the ionizing is the greatest. Ion drift accounts for a small fraction of the separation distance between the electron and ion distribution peaks.

Starting near a formation time of 2.4 μ-sec torr (not shown) the RW curves become progressively less sharply peaked than those of the approximate

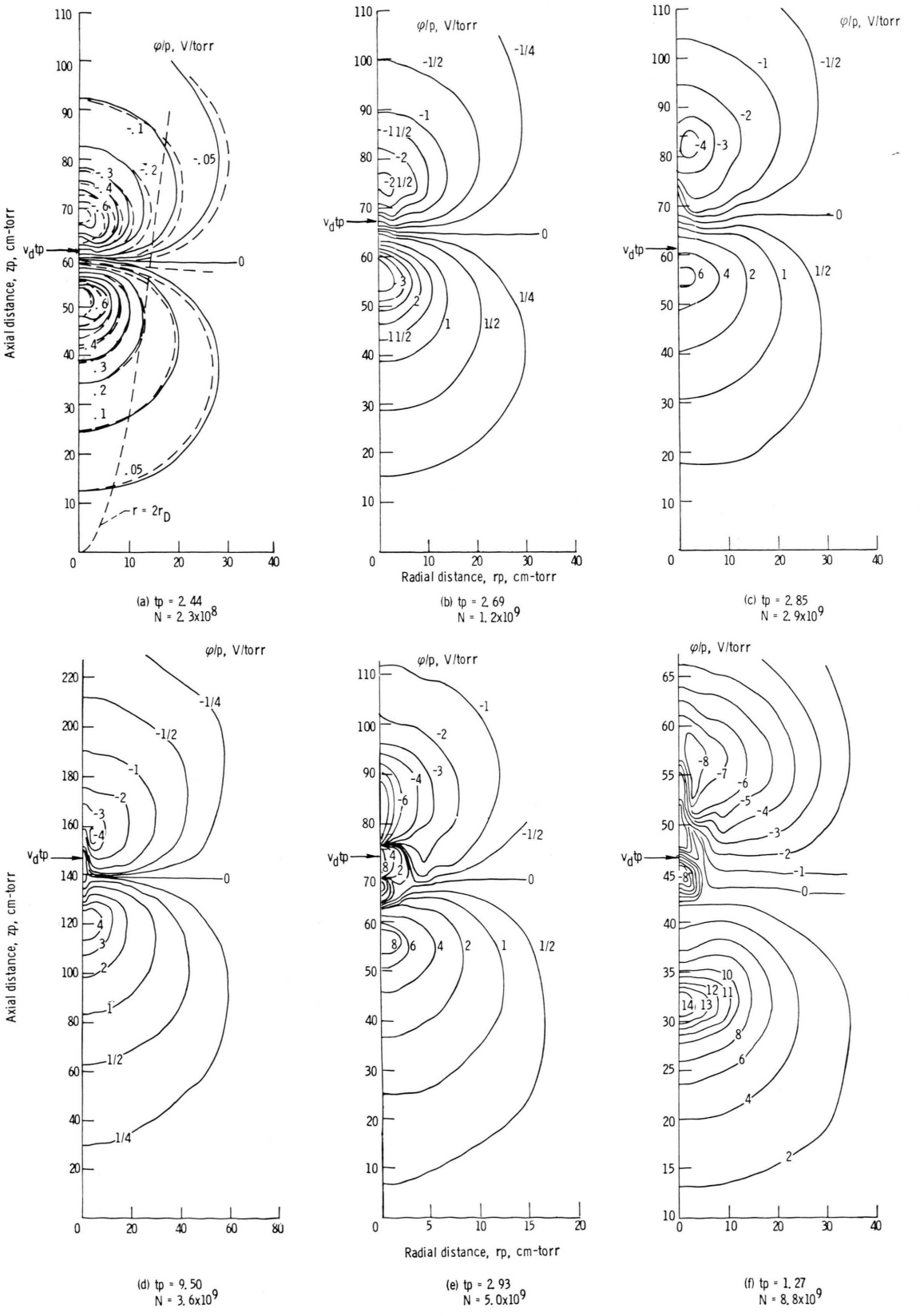

(a) t_p = 2.44, N = 2.3x10^8

(b) t_p = 2.69, N = 1.2x10^9

(c) t_p = 2.85, N = 2.9x10^9

(d) t_p = 9.50, N = 3.6x10^9

(e) t_p = 2.93, N = 5.0x10^9

(f) t_p = 1.27, N = 8.8x10^9

theory, especially for the z component of the distributions. (The dot-dash lines on Figs. 7 and 8 do not represent theory but are merely fairings of the RW results.) When a tp of 2.7 μ-sec torr is reached the z distribution starts to neck down at a z location somewhat less than $v_d t$. This is evident on Figure 8(b). Note that this is consistent with the computer plots of Fig. 5 which show a tendency for the electron swarm to separate into two zones.

Starting also at about a tp of 2.7 μ-sec torr, and shown later on Fig. 7(b), the radial marginal distribution has an increased concentration of both charge species near the axis as well as a spreading of the outer parts of the curve to radial distances beyond the theoretical curve. As time continues the trends become more pronounced with a sharp peak forming near the axis and near $v_d t$ in the radial and axial distributions, respectively. This zone is apparent in the last computer plot of Figure 5. By this time the induced internal electric field has exceeded the magnitude of the external field in this region.

Contour plots of the induced electrostatic potential, Φ, are shown in Figure 9. Patterns of Φ lines are shown in the early and intermediate stages of avalanche development in parts (a), (b), and (c) for an external field of 30 V/cm-torr. The contours are next shown near final stage of development for three external field strengths in parts (d), (e), and (f).

During early formation periods, the $\Phi = 0$ line is located near a zp station equal to $v_d tp$. The lines of constant Φ form sets of approximately circular contours about a region of maximum Φ located at an axial station less than $v_d tp$ and a region of minimum Φ at a zp greater than $v_d tp$. Constant coefficient theory [Eqs. (A10) and (A12) of the Appendix] agrees well with RW results as shown by dashed lines in part (a).

As formation time continues, the region of minimum Φ moves to slightly higher radii [Figs. 9(c) and (d)]. Comparison with Fig. 5 shows that the extrema regions and the distance between them is essentially the space covered by the electron swarm.

In the final stages of development the regions of extrema become more erratic and increase in number for all three E/p values.

The internal electric field in the avalanche head is generally predicted to be directed inward toward the center (Raether [8]) forcing the electrons outward; whereas the internal field in the trailing zone, being rich in ions, is predicted to be outward tending to force the electrons inward. This general pattern is observed in the present study only during the early formation period where the extrema of the field strength are both located on the avalanche axis. It is the local extrema regions which are decisive in the avalanche behavior.

The contour lines about and in the near vicinity of the regions of extrema often have two or more inflection points oriented such that they indicate enhanced gradients of Φ in the radial direction. During the latter stages of avalanche formation the radial electric field component, E_r, is found to grow more rapidly than the axial component. A plot of E_r/p versus axial distance in the region of extrema is shown in Fig. 10 at two radial locations near the axis and at various formation times. The external field here is 30 V/cm-torr.

At low tp the radial electric field has an approximately sinusoidal variation as zp increases over the span of the electron swarm. The variation of E_r with z at the inner radial location of Fig. 10 is more erratic, and indicates a tendency of local charge build-up and relaxation at z values between the two initial extrema. This may be an indication of instability caused by the exponential dependence of α_T/p on E/p. The restoring, or stabilizing influence is primarily the drift of electrons in response to the local electric field. At formation time of 2.93 μ-sec torr the field at the inner radius increases so abruptly that the assumption of axial symmetry can no longer be justified and the calculations were terminated.

Another indicator of the influence of the internal electric field is the effective Townsend ionization coefficient, defined here as

$$(\alpha_T/p)_{\text{eff}} = (v_d\, tp)^{-1} \ln (N/N_0) .$$

A retardation of avalanche growth below that calcalculated with a constant α_T/p equal to that at $tp = 0$ is usually predicted in the literature [9, 10] Such an effect is observed in the present results, as shown in

Fig. 9. Contour plots of induced electrostatic potential, Φ/p, V/torr. Parts (a), (b), and (c) are a development of one avalanche at three formation times, tp, given in microseconds. Here $E/p = 30$ V/cm-torr. Parts (d), (e), and (f) describe three different avalanches, at external fields of 20, 30, and 40 V/cm-torr, but all at a comparable final stage of development. The dashed contour lines in part (a) are from constant coefficient theory whereas the solid lines represent RW results.

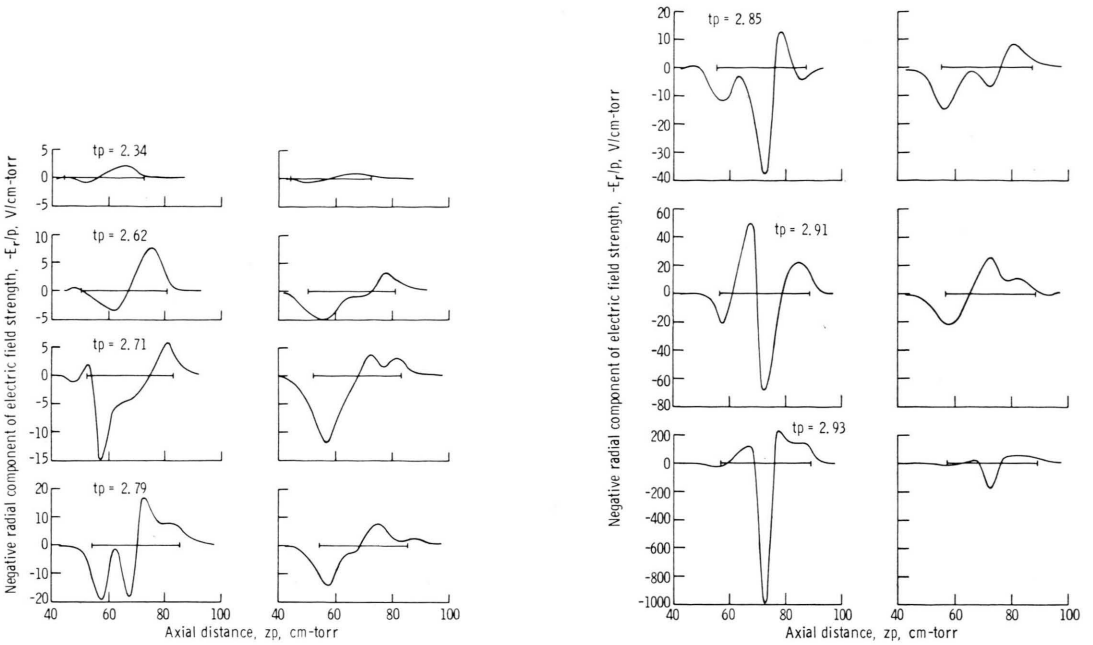

Fig. 10. Buildup of the radial component of the induced electric field in the region of extrema. Plots on the left are at a radial distance, $r\,p$, of 0.83 cm-torr from the avalanche axis, and plots on the right are for a $r\,p$ of 2.50 cm-torr. The horizontal lines illustrate the axial distance $\pm 4\,p\sqrt{D\,t}$ from $v_d\,t\,p$, which is the approximate axial distance covered by the electron swarm. 30 V/cm-torr.

Fig. 11, over about one-third of the formation time. This is due primarily to the ions lagging behind the electrons and causing an internal electric field which opposes the external field. In a later stage of development, however, the high field strengths discussed previously cause local increases in α_T/p which more than offset the retardation process, and $(\alpha_T/p)_{eff}$ sharply increases. A plot of $(\alpha_T/p)_{eff}$ versus N is given in Figure 11 (b). The general trends are quite consistent with the experimentally obtained results of Raether [8] for nitrogen. The abrupt increases in growth occur at formations of $e^{21.7}$, $e^{22.1}$, and $e^{22.7}$ ions which somewhat surpass the estimate of e^{20} for breakdown of Raether [4].

Use of the $(\alpha_T/p)_{eff}$ of Fig. 11 in place of the value of α_T/p at the beginning of the macroscopic calculations in Eqs. (A7) and (A9) of the Appendix gave little change in the theoretical ion marginal

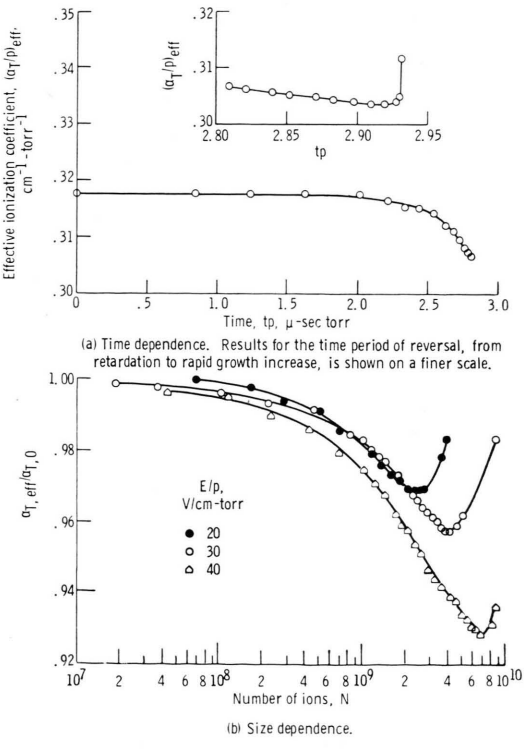

Fig. 11. Influence of the induced electric field on the effective Townsend ionization coefficient, $\alpha_{T,\,eff}$. The value of α_T used at the start of macroscopic RW calculations is denoted by $\alpha_{T,\,0}$.

(a) Time dependence. Results for the time period of reversal, from retardation to rapid growth increase, is shown on a finer scale.

(b) Size dependence. ⟶

distribution of Figs. 7 and 8. Use of $(\alpha_T/p)_{eff}$ in the electrostatic potential calculation of Eqs. (A10) and (A12), however, noticeably improved agreement between the constant coefficient theory and the RW results in the intermediate time periods.

The assumption that step size has only a weak spacial dependence, used in the derivation of Eq. (5) can now be further appraised. The ratio of step size, $\sqrt{(\Delta x)^2}$, to the step size at $z=0$ is plotted against $z\,p$ at a low $r\,p$ and a high $t\,p$ where the internal field, and thus transport coefficients, undergo extreme variations. This is compared to the dependence of other quantities entering the macroscopic RW calculations; the z component of bias, $\beta_z = P_z^+ - P_z^-$, and the probability of ionization, P_{ion}, in Figure 12. Step size is shown to be quite insensitive to distance, especially compared to the large changes experienced in the other two RW quantities.

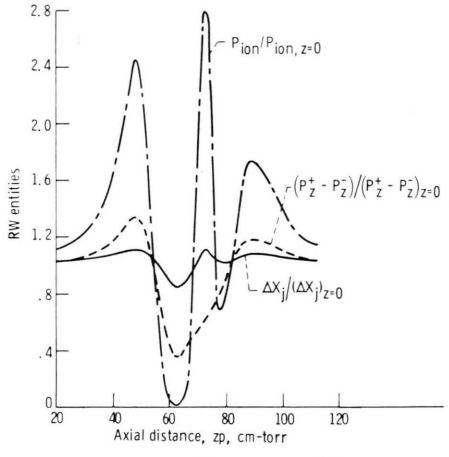

Fig. 12. Spatial variation of step size, ΔX_j; z component of bias, $P_z^+ - P_z^-$; and probability of ionization, P_{ion}. Radial distance from avalanche axis, $r\,p$, is 0.83 cm-torr. Formation time, $t\,p$, is 2.85 μ-sec torr. $E/p = 30$ V/cm torr.

Conclusions

The results of detailed random walks utilizing microscopic simulation of the electron trajectories in an avalanche in helium show that the electron transport coefficients relax to local equilibrium values in approximately one-hundredth of the formation time of a fully developed avalanche. This enables the use of a RW-on-a-grid concept for further study, with considerable reduction in computer time expenditure. A self-consistent avalanche solution accounting for collective long range Coulomb interactions as well as short range elastic and inelastic collisions is in turn made possible, requiring only a simple repetitious procedure.

Results obtained by this method at E/p values of 20, 30, and 40 V/cm-torr show that the induced internal electrostatic pattern in its early stage of formation has minimum and maximum values of potential, Φ, on the avalanche axis. The axial distance over which large Φ gradients appear is essentially that spanned by the electron swarm. As avalanche growth continues, the minimum Φ region moves to slightly higher radii. Within the separation distance between these two extrema, several other large Φ-gradient zones form in a manner which appears to be random in time.

In the final stage of development studied the induced internal electric field abruptly increases far beyond the magnitude of the external field.

The tail region behind the electron swarm, has a positive charge which opposes the external field. This tends to reduce the effective ionization coefficient, which is an indicator of the avalanche growth. At the time of the abrupt increase of the magnitudes of the internal field strength, the electron and ion formation rate in the region of the Φ extrema increases to the extent that it offsets the growth retardation in the tail region. The effective ionization coefficient then sharply increases.

Theory based on constant transport coefficients gives good results only in the early formation periods of the avalanche where induced internal electric fields are much less than the external fields. Here, electron and ion density distributions, as well as the general contours of the internal electrostatic potential are quite satisfactory. Some noticeable improvement in theoretical Φ contours is obtained by replacing Townsend's first ionization coefficient based on the external field by the effective ionization coefficient for the formation time of interest.

Appendix — Approximate Analytical Solutions of Descriptive Differential Equations

Ficks law for the flux of electrons about a mean (drift) velocity, v_d, due to diffusion is [11]

$$n_e(\overline{v} - v_d) = -D\nabla n_e .$$

Substituting this into the continuity equation,

$$\partial n_e/\partial t + \nabla \cdot n_e \overline{v} = \alpha_T v_d n_e ,$$

gives the electron transport equation

$$\partial n_e/\partial t = -\nabla\cdot n_e \boldsymbol{v}_d + \nabla\cdot(D\nabla n_e) + \alpha_T v_d n_e . \tag{A1}$$

The corresponding equation for ions, which have a negligible random velocity is

$$\partial n_i/\partial t = -\nabla\cdot n_i \boldsymbol{v}_{d,i} + \alpha_T v_d n_e . \tag{A2}$$

Equations (A1) and (A2) are coupled through Poisson's equation,

$$\nabla^2 \Phi = -4\pi e(n_i - n_e) ,$$

and the dependence of the transport coefficients on the electric field vector which is equal to $-\nabla\Phi$ plus the external electric field.

Density distributions. – For constant coefficients Eqs. (A1) and (A2) can be solved immediately. The electron density is

$$n_e = (4\pi D t)^{-3/2} \exp\{\alpha_T v_d t - [r^2 + (z - v_d t)^2]/4 D t\} \tag{A3}$$

in cylindrical coordinates with azimuthal symmetry. Here the avalanche is assumed to start from one electron. Assuming that ion drift is negligible, Eq. (A2) gives

$$n_i = \alpha_T v_d \int_0^t n_e \, dt' . \tag{A4}$$

Making use of (A3) there results

$$n_i = \alpha_T v_d \int_0^t (4\pi D t)^{-3/2} \exp\{\alpha_T v_d t' - [r^2 + (z - v_d t')^2]/4 D t'\} \, dt' . \tag{A5}$$

Marginal distributions are often used to reduce the number of variables required for plotting results. Integrating densities, n_e and n_i, over r and θ gives the marginal distributions, $n_{e,z}$ and $n_{i,z}$, in z, respectively, as

$$n_{e,z} = \int_0^\infty \int_0^{2\pi} n_e r \, d\theta \, dr = (4\pi D t)^{-1/2} \exp[\alpha_T v_d t - (z - v_d t)^2/4 D t] \tag{A6}$$

and

$$n_{i,z} = \alpha_T v_d \pi^{-1/2} \int_0^t (4 D t')^{-1/2} \exp\{\alpha_T v_d t' - (z - v_d t')^2/4 D t'] dt' , \tag{A7}$$

where use was made of (A3) and (A4). The corresponding marginal density distributions in r are as follows. For electrons

$$n_{e,r} = \int_0^\infty \int_0^{2\pi} n_e r \, d\theta \, dz = (4 D t)^{-1} r[1 + \mathrm{erf}(v_d t/\sqrt{4 D t})] \cdot \exp(\alpha_T v_d t - r^2/4 D t) .$$

For times of interest $\mathrm{erf}(v_d t/\sqrt{4 D t}) \approx 1$ and thus

$$n_{e,r} \cong (2 D t)^{-1} r \exp(\alpha_T v_d t - r^2/4 D t) . \tag{A8}$$

Using this result in (A4) gives

$$n_{i,r} = \alpha_T v_d r \int_0^t (2 D t')^{-1} \exp(\alpha_T v_d t' - r^2/4 D t') \, dt' . \tag{A9}$$

Equations (A6) through (A9) can be normalized by dividing by $\exp(\alpha_T v_d t)$.

Potential distributions. – When the assumption of constant transport coefficients applies, the electrons diffuse as a spherically symmetric swarm, the center of which is at $z = v_d t$ on the avalanche axis of symmetry. The contribution of a spherical electron distribution to the internal (induced) electrostatic potential, $\Phi = \Phi_e + \Phi_i$, is

$$\Phi_e(R, t) = 4\pi e R^{-1} \int_0^R R'^2 n_e(R', t) \, dR' + 4\pi e \int_R^\infty R' n_e(R', t) \, dR' ,$$

where R is radial distance in the spherical (avalanche space) system. Using Eq. (A3) and integrating gives

$$\Phi_e(R, t) = -e R^{-1} \mathrm{erf}(R/\sqrt{4 D t}) \exp(\alpha_T v_d t) . \tag{A10}$$

Equation (A4) indicates that the internal potential, Φ_i, due to the ion distribution can be expressed in terms of Φ_e as

$$\Phi_i = -\alpha_T v_d \int_0^t \Phi_e \, dt' . \tag{A11}$$

Changing Eq. (A10) to cylindrical coordinates in laboratory space, and substituting the resulting expression into (A11) gives

$$\Phi_i(r, z, t) = \alpha_T v_d e \int_0^t \frac{\exp(\alpha_T v_d t')}{\sqrt{r^2 + (z - v_d t')^2}} \cdot \mathrm{erf}\{[r^2 + (z - v_d t')^2]/4 D t'\}^{1/2} \, dt' . \tag{A12}$$

[1] G. W. Englert, Z. Naturforsch. **26 a**, 836 [1971].
[2] G. W. Englert, Appl. Sci. Res. **25**, 201 [1971].
[3] G. W. Englert, Nucl. Fusion **10**, 361 [1970].
[4] H. Rather, Electron Avalanches and Breakdown in Gases, Butterworth, Washington, D.C., 1964.
[5] L. B. Loeb, Basic Processes of Gaseous Electronics, University of California Press, Berkeley, and Los Angeles, 1961.
[6] Pressure, p, is referenced to 0 °C, thus $p=n/3.54\times10^{16}$ where n is the density of background particles.
[7] Equilibrium coefficients for the avalanches are slightly below the values of Reference 1. This can be explained as follows. After an ionization event there results two electrons to share the available energy which is equal to the initial energy of the impacting electrons minus V_i. Both of the resulting relatively low energy electrons are kept in the avalanche calculations whereas only one is kept when a fixed number of test particles are considered [1]. This slight difference of results is less detectable for drift and diffusion coefficient and is considered negligible for purposes herein.
[8] H. Rather, Comptes Rendus de la VI Conf. Int. sur les Phen. D'Ioniz. dans les Gaz. Paris **II**, 305 [1963].
[9] K. J. Schmidt-Tiedemann, Z. Naturforsch. **14 a**, 989 [1959].
[10] A. E. D. Heylen, Proc. of Seventh Int. Conf. on Phen. in Ionized Gases **1**, 563 [1963].
[11] J. Crank, The Mathematics of Diffusion, Oxford at the Clarendon Press, 1956.